Available online at www.sciencedirect.com
ScienceDirect
Physica D 223 (2006) 36–53
PHYSICA D
www.elsevier.com/locate/physd

Chaotic advection in the restricted four-vortex problem on a sphere☆

Paul K. Newton, Shane D. Ross*

Department of Aerospace and Mechanical Engineering, University of Southern California, Los Angeles, CA 90089, USA

Received 31 March 2005; received in revised form 17 April 2006; accepted 11 August 2006
Available online 9 October 2006
Communicated by I. Mezic

Abstract

The chaotic advection of tracer particles in the field of a perturbed latitudinal ring of point vortices on a sphere is considered. We consider a restricted four-vortex problem where three vortices have equal strength, while the fourth has strength zero. The equal-strength vortices are initially spaced evenly on a ring of fixed latitude in the northern hemisphere. The equilateral triangle formed by the vortices is known to be a nonlinearly stable relative equilibrium configuration. When perturbed, the vortex motion induces chaotic particle advection analyzed by means of stroboscopic Poincaré maps as a function of the dimensionless energy of the system, which can be related to the size of the perturbation from equilibrium. A critical energy is identified which separates the vortex motion into two distinct dynamical regimes. For energies below critical, the vortices undergo periodic partner exchange while retaining their relative orientation. For values above critical, the relative orientation of the vortices changes throughout the periodic cycle. We consider how the streamline topologies bifurcate both as a function of the energy and during the course of their evolution, as well as the role that the evolution of instantaneous streamline structures plays in the mixing and transport of particles. The geometric extent of the mixing region on the full sphere is considered (measured as a percentage of the surface area of the sphere) and dynamical properties in the region, such as mixing and stretching rates as well as computational evidence of ergodicity, are obtained. Global mixing on the sphere does not seem to increase monotonically with energy, but appears to be maximized for values near critical.

Keywords: Chaotic advection; Vortex ring; Particle transport; Ergodicity; Mixing

1. Introduction

The dynamics of point vortices moving on the surface of a sphere is not as well understood as the corresponding planar problem, despite the fact that the model is very relevant both in atmospheric and oceanographic settings when one considers large-scale phenomena where the spherical geometry of the Earth's surface becomes important. The full spherical geometry, as opposed to its β-plane approximation, is particularly important when considering global streamline patterns generated by a given vorticity distribution, since the Poincaré index theorem provides an important constraint on allowable patterns [24]. These patterns, in turn, provide the dynamical templates by which one can begin to understand the chaotic advection of particles in a vortex-dominated flow, a topic closely related to the dynamics of point vortices. The problem motivating the model studied in this paper is the role the polar vortex plays in the transport and dispersion of stratospheric particles [1,16]. It has been recognized that transport in the stratosphere is dominated by advection from large-scale structures and that, on a time scale of days to weeks, the transport is quasi-horizontal, along isentropic surfaces [15], i.e., on two-dimensional layers. Thus chaotic advection in a vortex-dominated flow on a spherical shell offers a useful paradigm for understanding how complicated spatial structures can arise and evolve. Additional important geophysical effects such as rotation [18,36] or vertical density stratification further complicate these dynamical processes but are not considered here.

In this paper, we formulate and study the simplest model in which one can distribute vorticity in order to understand its ability to transport and mix particles. Our overriding goal

☆ This research was supported by NSF-DMS 9800797 and NSF-DMS 0203581 (PN), and NSF-DMS 0402842 (SR).

* Corresponding address: Engineering Science and Mechanics, Virginia Polytechnic Institute and State University, Mail Code 0219, Blacksburg, VA 24061, USA. Tel.: +1 540 231 1616; fax: +1 540 231 4574.
E-mail address: sdross@vt.edu (S.D. Ross).

0167-2789/$ - see front matter © 2006 Elsevier B.V. All rights reserved.
doi:10.1016/j.physd.2006.08.012

is to identify and develop specific initial configurations whose streamline patterns and evolution are topologically similar to realistic atmospheric events, as identified in data sets. This is motivated by the observation, as shown in the thesis of [42], that when global weather patterns are viewed as daily or weekly averages, their streamline patterns are surprisingly simple. In fact, if one disregards their dynamics, their topologies are typically not much more complex than those that the three- or four-vortex problem is capable of producing, as categorized in [24]. Our focus in this paper, therefore, is on the chaotic advection of particles in the presence of three vortices — the fewest necessary to generate chaotic particle trajectories.

In analogy with terminology borrowed from the gravitational N-body literature, we study a configuration associated with a restricted four-vortex problem where three vortices have equal strength, while the fourth vortex has strength zero, and hence is a passively advected particle. In celestial mechanics, two bodies are necessary to generate chaotic particle advection [25]. The study of particle transport in a system of N massive bodies can be well approximated as a series of coupled restricted three-body problems [13]. This analogy may carry over, with modification, to vortex dynamics, where particle transport in an N-vortex system can be decomposed into series of restricted four-vortex problems.

The three-vortex problem on the sphere, a completely integrable problem, is now well understood [6–8,22–24,40]. Our interest is in the motion of three identical vortices, evenly spaced on a constant latitudinal ring in the northern hemisphere. This configuration is a relative equilibrium configuration [30] that is linearly [38] and nonlinearly stable [37] (see [2,4] for a recent discussion). The vortex motion is parametrized by a characteristic length scale and a vortex interaction energy, which naturally divides the phase space into two regimes in which one would expect the advected particle motion to share certain dynamical characteristics. These characteristics are topological and depend on how the vortices wrap around one another during their evolution, which can be described using braids [10].

The equilateral triangle is perturbed to an isosceles triangle by a deformation parameter ε which takes the configuration from an initial equilateral shape ($\varepsilon = 0$), to an isosceles triangle ($\varepsilon > 0$), ultimately to the singular limit of a two-vortex configuration ($\varepsilon = 1$) in which one of the vortices has twice the strength of the other. The vortex motion generally consists of quasi-periodic orbits.

We then consider the motion of passive fluid particles in this system, which can be reduced to a periodically forced Hamiltonian dynamical system, a system with $1\frac{1}{2}$ degrees of freedom. The vortices play the role of stirrers, effectively mixing the fluid in a multiply connected region of the sphere we call the mixing region, following the terminology of [34, 26] which studied chaotic advection in the presence of three vortices in the plane. We consider the extent of the mixing region as a percentage of the surface area of the sphere, the speed with which particles are transported, and the role that the evolution of instantaneous streamline structures plays in this complex process. The streamlines reveal that the two regimes of motion correspond to (a) a situation in which there is sequential pairing between the three vortices, i.e., partner exchange, and (b) a situation where two of the vortices form a pair which rotate around each other for all time, a $2+1$ state. It is the first of these regimes that provides for the most efficient mixing, particularly for energies near a critical value corresponding to a great circle state, an unstable equilibrium of the three vortices.

2. The motion of three identical vortices on a sphere

It is convenient to formulate the three-vortex problem on the unit sphere in Cartesian coordinates, where the vector $\mathbf{x}_i = (x_i, y_i, z_i) \in \mathbb{R}^3$ points from the center of the unit sphere to the point vortex with strength $\Gamma_i \in \mathbb{R}$ on the spherical surface. We will take the vortices to be of the same positive strength, i.e., $\Gamma_1 = \Gamma_2 = \Gamma_3 = \Gamma > 0$. Each point vortex moves under the collective influence of all the others, and the equations of motion are (from [35])

$$\dot{\mathbf{x}}_i = \frac{\Gamma}{2\pi} \sum_{j=1}^{3}{}' \frac{\mathbf{x}_j \times \mathbf{x}_i}{l_{ij}^2}, \quad i = 1, 2, 3, \tag{1}$$
$$\|\mathbf{x}_i\| = 1,$$

where the denominator in the summation is the square of the chord distance between vortices i and j,

$$l_{ij}^2 = \|\mathbf{x}_i - \mathbf{x}_j\|^2 = 2(1 - \mathbf{x}_i \cdot \mathbf{x}_j),$$

and the prime on the summation reminds us that the singular term $j = i$ is omitted. Initially, the vortices are located at the given positions $\mathbf{x}_i(0) \in \mathbb{R}^3$, $i = 1, 2, 3$.

If we use spherical coordinates (θ_i, ϕ_i) where the θ_i are co-latitudes and the ϕ_i are longitudes, the system (1) can be described as a Hamiltonian system with Hamiltonian

$$H = -\frac{\Gamma^2}{4\pi} \sum_{i<j} \log(l_{ij}^2). \tag{2}$$

With the coordinates $q_i = \sqrt{\Gamma}\phi_i$ and $p_i = \sqrt{\Gamma}\cos\theta_i$ the system is put in canonical form

$$\dot{q}_i = \frac{\partial H}{\partial p_i}, \qquad \dot{p}_i = -\frac{\partial H}{\partial q_i}, \quad i = 1, 2, 3.$$

Since the Hamiltonian, H, does not depend on time explicitly, its value is a constant of the motion.

The center of vorticity vector is also conserved for the system, given by

$$\mathbf{c} = \frac{\mathbf{M}}{S}, \tag{3}$$

where

$$\mathbf{M} = \sum_{i}^{3} \Gamma_i \mathbf{x}_i = \Gamma \sum_{i}^{3} \mathbf{x}_i$$

is the moment of vorticity and $S = \sum_i^3 \Gamma_i = 3\Gamma$ is the total vorticity.

2.1. Relative dynamics

Following [22], the equations of the relative dynamics of the vortices can be derived from the original system (1) and are given by

$$\frac{\mathrm{d}}{\mathrm{d}t}(l_{12}^2) = \frac{\Gamma V}{\pi}\left(\frac{1}{l_{23}^2} - \frac{1}{l_{31}^2}\right) \tag{4}$$

$$\frac{\mathrm{d}}{\mathrm{d}t}(l_{23}^2) = \frac{\Gamma V}{\pi}\left(\frac{1}{l_{31}^2} - \frac{1}{l_{12}^2}\right) \tag{5}$$

$$\frac{\mathrm{d}}{\mathrm{d}t}(l_{31}^2) = \frac{\Gamma V}{\pi}\left(\frac{1}{l_{12}^2} - \frac{1}{l_{23}^2}\right), \tag{6}$$

where V is the parallelepiped volume formed by the vectors $\mathbf{x}_1, \mathbf{x}_2, \mathbf{x}_3$, as obtained from

$$V = \mathbf{x}_1 \cdot (\mathbf{x}_2 \times \mathbf{x}_3).$$

The system (4)–(6) has two fundamental invariants of motion

$$C_1 = \Gamma^2 \sum_{i<j} l_{ij}^2, \tag{7}$$

$$C_2' = -\frac{\Gamma^2}{4\pi} \sum_{i<j} \log(l_{ij}^2), \tag{8}$$

(arising from conservation of momentum and energy), where the second quantity can be usefully exponentiated and written as

$$C_2 = \exp(-4\pi C_2'/\Gamma^3) = (l_{12}^2 l_{23}^2 l_{31}^2)^{1/\Gamma}. \tag{9}$$

For the identical vortices, it is convenient to introduce scaled variables, for comparison with [34]. First, assuming $C_1 \neq 0$, we can introduce an invariant characteristic length scale l, where

$$\begin{aligned} l^2 &= \frac{C_1}{3\Gamma^2}, \\ &= \frac{1}{3}(l_{12}^2 + l_{23}^2 + l_{31}^2). \end{aligned}$$

The scaled length variables, from [35], are then

$$b_1 = \frac{l_{23}^2}{l^2}, \qquad b_2 = \frac{l_{31}^2}{l^2}, \qquad b_3 = \frac{l_{12}^2}{l^2}. \tag{10}$$

The equation for the invariant (7) then becomes

$$b_1 + b_2 + b_3 = 3.$$

In the scaled length variables, the second invariant (8), in units of $\Gamma^2/2\pi$, becomes

$$\begin{aligned} C_2' &= -\frac{1}{2}(\log b_1 + \log b_2 + \log b_3), \\ &= -\frac{1}{2}\log(b_1 b_2 b_3), \\ &= -\log\left(\frac{l_{12} l_{23} l_{31}}{l^3}\right). \end{aligned}$$

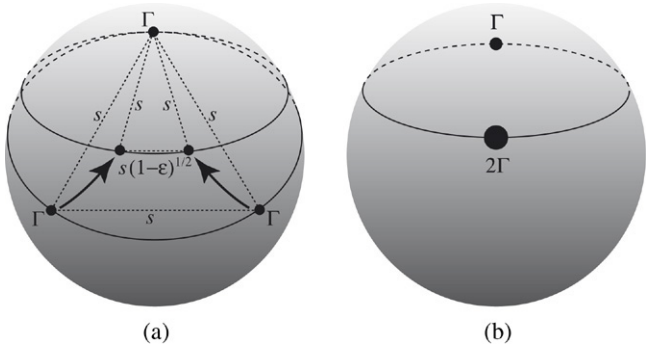

Fig. 1. (a) The initial positions of the three vortices of equal positive strength Γ is shown on the unit sphere. The initial distances between the vortices form an isosceles triangle of sides s, s, and $s\sqrt{1-\varepsilon}$, with the equilateral configuration for $\varepsilon = 0$. (b) As $\varepsilon \to 1$, two of the vortices merge and we have a two-vortex problem where the vortices have strengths Γ and 2Γ.

This is the same as the Hamiltonian (2) written in the scaled units, and is the same as the value for the vortex interaction energy E used by [34] for the corresponding planar problem,

$$E = -\log\left(\frac{l_{12} l_{23} l_{31}}{l^3}\right). \tag{11}$$

In the limit when the vortices are close to each other compared to the radius of the sphere ($l \ll 1$), we expect their behavior to be the same as in the planar problem. We will treat the dimensionless energy, E, as a key parameter of the system.

2.2. The overall motion as a function of energy and length scale

Unlike the planar problem, the overall motion of three identical vortices on the sphere is a function of more than just the energy E. This is because the geometry of the sphere introduces a new length scale parameter $s \in (0, 2)$. We will consider the three vortices of unit strength (i.e., $\Gamma = 1$) to be initially placed on the sphere in a triangular configuration, shown in Fig. 1(a), such that

$$\begin{aligned} l_{12}(0) &= l_{31}(0) = s, \\ l_{23}(0) &= s\sqrt{1-\varepsilon}, \end{aligned}$$

where the perturbation away from an equilateral triangle is parametrized by the parameter $\varepsilon \in [0, 1]$, which is a function of the energy, i.e., $\varepsilon = \varepsilon(E)$. Here E and ε are related via

$$E = -\frac{1}{2}\log\left(\frac{(1-\varepsilon)}{\left(1-\frac{\varepsilon}{3}\right)^3}\right), \tag{12}$$

since $l = s\sqrt{1-\frac{\varepsilon}{3}}$. Note that $E \in [0, \infty)$ for $\varepsilon \in [0, 1]$. The parameter s can be related to the co-latitude. For $\varepsilon = 0$ we have $s = \sqrt{3}\sin\theta$. But as ε increases, the co-latitude changes, as shown in Fig. 1(a). Fig. 2 shows the streamline patterns associated with the triangular configurations of Fig. 1 as a function of the energy for $s = 1$. Each case shown represents a distinct topology which is made up of the fundamental building blocks identified in Kidambi and Newton [24].

The overall dynamics of the three identical vortices can be decomposed into a superposition of relative vortex motion

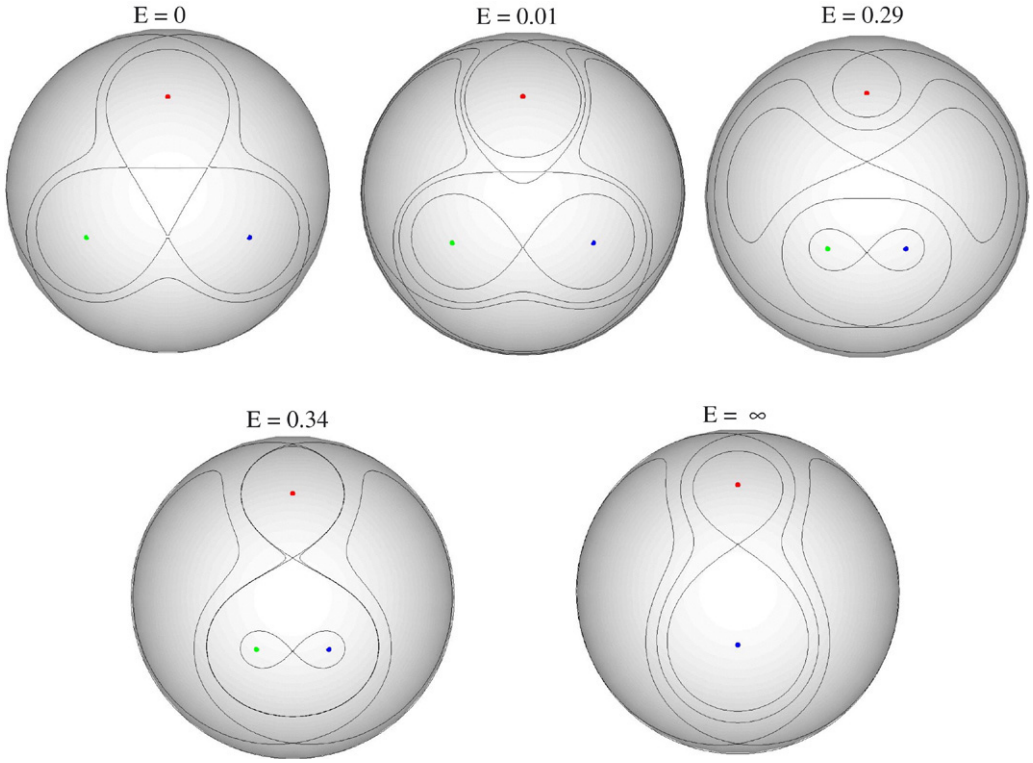

Fig. 2. The streamline topologies for $t = \mathrm{mod}(t, T)$ as a function of energy for $s = 1$. Note that each of the patterns is topologically distinct.

along with a global rotation of the whole system around the center of vorticity (3). The relative motion, described by the dynamical equations (4)–(6), is periodic with period T and frequency $\omega_{\mathrm{rel}} = 2\pi/T$. The global rotation can be characterized by measuring the angular displacement $\Delta\phi_0$ about the center of vorticity between two configurations separated by time T. The frequency of the global rotation can be defined as

$$\omega_{\mathrm{glob}} = \frac{\Delta\phi_0}{T}.$$

The pair of frequencies $(\omega_{\mathrm{rel}}, \omega_{\mathrm{glob}})$ depend on the parameters (s, E) and are generally incommensurate, implying that the overall vortex motion is quasi-periodic. In Fig. 3 we show the energy dependence of the frequencies when $s = 1$ which were obtained by numerical integration of Eq. (1). We note the agreement of the features of these curves with the similar curve obtained in [34] for the plane, which corresponds to the $s \to 0$ case.

To gain a global view of the motions possible, we can consider the bifurcation diagram of the system in (s, E) space. For $s \in (0, \sqrt{3})$, there is a single critical energy, $E_c > 0$, which separates two regimes of motion: partner exchange for $E < E_c$ and a $2 + 1$ regime for $E > E_c$.

The regimes can be defined by considering the time profiles of l_{12}, l_{23}, and l_{31} over one period of relative motion. In the partner exchange regime, the three curves are related by phase shifts, $l_{31}(t) = l_{23}(t - T/3) = l_{12}(t + T/3)$. The evolution of the instantaneous streamlines reveal that initially vortices 2 and 3 form a close pair with a figure of eight streamline connecting them. At $t = T/6$, a partner exchange takes place. Vortices 3 and 1 then form a close pair, connected by a figure of eight streamline in the interval $t \in (T/6, T/3)$, and so forth. The vortices never pass through a great circle state for this regime.

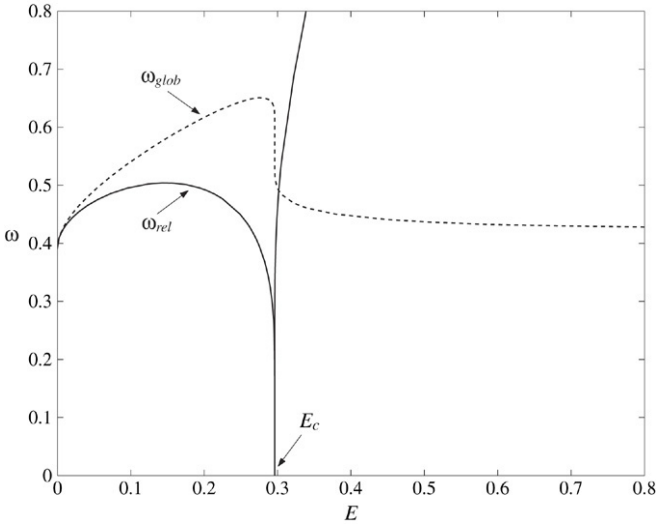

Fig. 3. Energy dependence of the angular velocity corresponding to the global rotating (ω_{glob}) and relative (ω_{rel}) motion of a system of three identical vortices when $s = 1$. The right branch of $\omega_{\mathrm{rel}}(E)$ grows monotonically in the region not shown, i.e., for $\omega > 0.8$.

In the $2 + 1$ regime, vortices 2 and 3 form a close pair for all time and we have $l_{31}(t) = l_{12}(t + T/2)$ and $\min_{t\in[0,T)} l_{31}(t) > \max_{t\in[0,T)} l_{23}(t)$. The vortices pass through a great circle state twice every period of relative motion.

The critical value $E = E_c$ corresponds to a special kind of motion, a convergence to a great circle state of the vortices,

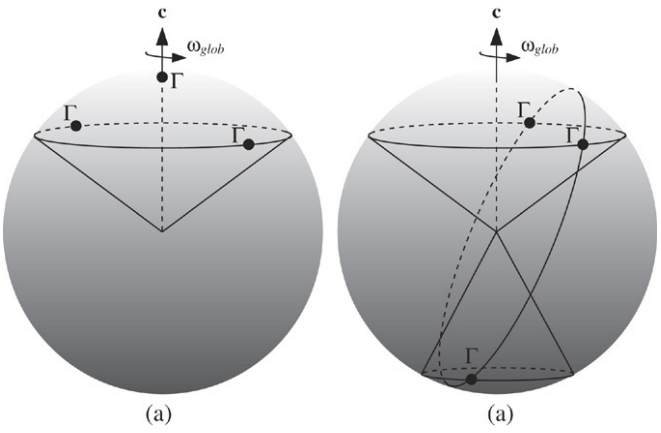

Fig. 4. (a) The unstable relative equilibria at the critical value of energy which separates the partner exchange and 2+1 regimes of vortex motion. The vortices lie along a great circle, and rotate about the central vortex located at the north pole, the center of vorticity vector **c**. (b) The minimum energy unstable relative equilibria correspond to another kind of constant rotational motion where all vortices are along a great circle. The vortices move on cones around the center of vorticity vector **c**. The top two vortices are on the same cone. Note that although $|\mathbf{c}| \leq 1$ we show it coming out of the sphere for illustrative convenience.

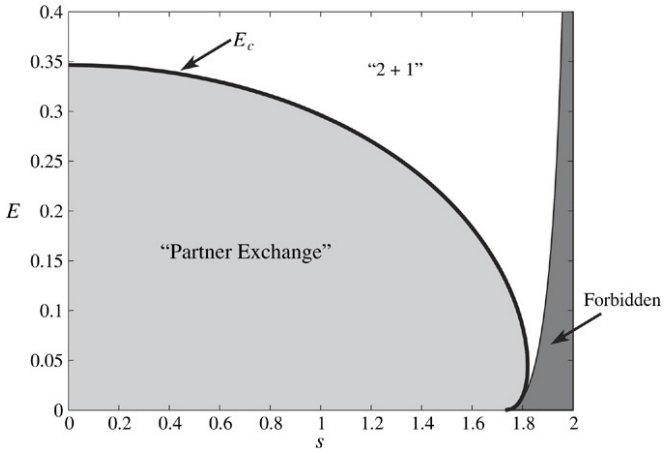

Fig. 5. The (s, E) plane can be partitioned into regions where the three vortices exhibit a partner exchange or 2+1 behavior. These regions are separated by the curve of critical energies E_c.

the spherical analogue of the collinear state for the planar problem. The motion of the vortices is an unstable relative equilibrium [37], with constant rotation around the central vortex located at the north pole as shown in Fig. 4(a). The value of E_c for the spherical problem changes with s, but asymptotes to $(\log 2)/2$ as $s \to 0$, corresponding to the planar problem [34].

Using the above criteria, we can compute the curve of critical energies starting with small s and using numerical continuation. The resulting curve is shown in Fig. 5. The curve of critical energy is double valued for some small range of s beginning at $\sqrt{3}$ and ending at $s = s^*$ where s^* is approximately 1.82034. For a given s in this range, we speak of the upper critical energy value as $E_c^{(u)}$ and the lower value as $E_c^{(l)}$. For $s > s^*$, there is no partner exchange regime, only the $2 + 1$ regime. Qualitatively speaking, we can understand this situation by considering the geometry of the vortices on the sphere. As s gets very close to 2 (the diameter of the sphere), the close pair will stay close to each other.

A forbidden regime (dark) is shown on the right side of the figure. For a given $s > \sqrt{3}$, there is a minimum $\varepsilon > 0$ (and thus minimum $E > 0$) needed for the three vortices to be on the sphere [5]. Any energy below this is not a possible configuration for the vortices. This minimum corresponds to a great circle state, distinct from the critical energy state(s) above, and is given simply by

$$\varepsilon_{\min} = s^2 - 3.$$

The situation is shown in Fig. 4(b). This minimum energy state is also a nondegenerate (i.e., $\mathbf{c} \neq 0$) relative equilibrium which is nonlinearly unstable [37].

We can summarize the bifurcation diagram as follows. For $s < \sqrt{3}$, we have a single branch of relative equilibria which are great circle states and unstable. At the point $(s, E) = (\sqrt{3}, 0)$, we have a fixed equilibrium equilateral triangle which is a degenerate (i.e., $\mathbf{c} = 0$) great circle state and nonlinearly stable [37]. Two branches of great circle equilibria are born at $(s, E) = (\sqrt{3}, 0)$ as s increases. The lowest branch is the minimum energy branch. The other branch is part of the previously discussed critical energy curve which separates the two vortex motion regimes, and corresponds to an unstable relative equilibrium great circle state. This branch of equilibria does not extend past $s = s^*$.

To illustrate the different motions as we vary E for a fixed value of s, let us restrict ourselves for the moment to the case $s < \sqrt{3}$. Beginning at $E = 0$, the vortices form an equilateral triangle of edge length s which rotates uniformly around the center of vorticity without relative motion, i.e., $\omega_{\text{rel}}(0) = \omega_{\text{glob}}(0)$, where

$$\omega_{\text{glob}}(0) = \frac{3}{2\pi s^2}\sqrt{1 - s^2/3}.$$

At small positive energies, the vortices exhibit an oscillation around the equilateral configuration, which to leading order in ε has the frequency

$$\omega_{\text{rel}}(E(\varepsilon)) = \frac{3}{2\pi s^2}\sqrt{1 - s^2/(3+\varepsilon)}\sqrt{\frac{1+\varepsilon/3}{1-\varepsilon}} \quad \text{for } \varepsilon \ll 1,$$

where E and ε are related by (12).

In general, for $0 < E < E_c$, the triangle spanned by the vortices oscillates between two isosceles triangles. This oscillation in the shape of the vortex triangle is accompanied by the cyclic permutation of the vortices. The system can never pass through a great circle configuration, so the orientation of the triangle remains unchanged in time, i.e., the vortices 1, 2, and 3 appear in anticlockwise order, viewed from the north pole. Because of this, the braid structure is trivial: there are no twists. In Fig. 6, we show the trajectories of the three vortices in a frame co-rotating around the center of vorticity with frequency $\omega_{\text{glob}}(E)$ for E just slightly below E_c.

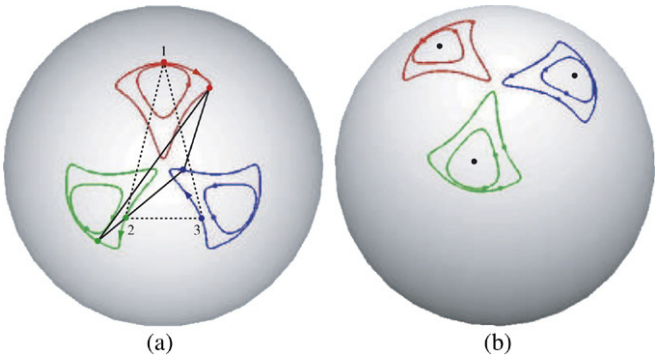

Fig. 6. (a) Trajectories of the three vortices on the sphere viewed from the co-rotating frame. The innermost curves are for $E = 0.13$ and the outermost curves are for $E = 0.29$, just below E_c. The triangles formed by the three vortices at $t = 0$ (dashed) and $t = T/4$ (solid) are shown for $E = 0.29$. (b) The same vortex trajectories on the sphere are shown from an angle to reveal the three-dimensionality of the curves. The central points are located at the vertices of the equilateral triangle configuration.

Fig. 6(a) shows trajectories of the three vortices on the sphere viewed from the co-rotating frame. Looking down at the north pole (recall the center of vorticity vector is aligned with the positive z-axis), the initial positions of the vortices are marked by a dot. There are two energy cases shown, both for $s = 1$. The trajectories are closed curves of period $T = 2\pi/\omega_{\text{rel}}(E)$ and the sense of motion on each curve is clockwise. The innermost curves are for $E = 0.13$. The positions at time $t = T/4$ are also shown as dots. The outermost curves are for $E = 0.29$ just below E_c. The dashed triangle is formed by the three vortices at $t = 0$, with the vortices numbered 1, 2, and 3. The triangle formed by the same vortices a quarter-cycle later ($t = T/4$) is shown as solid.

Fig. 6(b) shows the same closed curves from a different perspective to reveal the three-dimensionality of the curves. The equilateral triangle configuration in the rotating frame is shown as the dots. For all the specific cases of (s, E) given in this paper, the vortices always remain in the northern hemisphere. But as will be shown, for some cases an advected particle can wander through much of the southern hemisphere.

For $E_c < E < \infty$ the orientation of the triangle is no longer conserved and a new characteristic of the motion is that two vortices remain closer to each other than to the third one. The triangle spanned by the vortices oscillates between two identical isosceles triangles having different orientations due to the exchange of the two near vortices passing through the great circle state twice in one period of the relative motion. Because vortices 2 and 3 wind around each other, the braid of the three vortices is such that 2 and 3 have two 180° anticlockwise twists per period.

As $E \to \infty$ the two vortices tend to coalesce and the dynamics converge to the two-vortex problem where one of the vortices has double strength (see Fig. 1(b)), and the rotation period is

$$\omega_{\text{glob}}(\infty) = \frac{\|\mathbf{M}\|}{2\pi s^2} = \frac{3}{2\pi s^2}\sqrt{1 - 2s^2/9}.$$

3. Streamline topologies

The advection of passive tracer particles is determined by the underlying velocity field. A particle can be considered a vortex of zero strength with position $\mathbf{x} = (x, y, z) \in \mathbb{R}^3$ where $\|\mathbf{x}\| = 1$ constrains the particle to be on the sphere. The equations of motion for a particle on the sphere in the presence of three vortices of unit strength is

$$\dot{\mathbf{x}} = \frac{1}{2\pi}\sum_{j=1}^{3}\frac{\mathbf{x}_j \times \mathbf{x}}{l_j^2} \tag{13}$$

where the denominator in the summation is the square of the chord distance between the particle and vortex j,

$$l_j^2 = \|\mathbf{x} - \mathbf{x}_j\|^2 = 2(1 - \mathbf{x}\cdot\mathbf{x}_j).$$

Initially, the particle is located at the given position $\mathbf{x}(0) \in \mathbb{R}^3$. In spherical coordinates, the initial position is $(\theta(0), \phi(0)) \in S^2 \subset \mathbb{R}^3$.

3.1. Stereographic projection

It is useful to project the spherical equation (13) onto a plane so that the Hamiltonian for the particle can be written out and the instantaneous streamline topology can be determined. The change of variable

$$r = \tan\left(\frac{\theta}{2}\right),$$

results in a stereographic projection of the particle onto the extended complex plane $\mathcal{C}$ which is tangent to the sphere at the north pole. This point of tangency is at the origin of $\mathcal{C}$, while the south pole ($\theta = \pi$) maps to the point at infinity. The location of the particle $z \in \mathcal{C}$ is given by $z = x + \mathrm{i}y$ where

$$x = r\cos\phi,$$
$$y = r\sin\phi,$$

and similarly for the locations of the vortices, $z_j \in \mathcal{C}$, $j = 1, 2, 3$.

3.2. Rotating frame Hamiltonian for the particle

Without loss of generality, we align the center of vorticity $\mathbf{c}$ with the z-axis. The global rotation of the vortices is then around the z-axis with frequency ω_{glob}. In the rotating frame, the Hamiltonian for the particle motion projected onto $\mathcal{C}$ is

$$H_p = \frac{1}{4\pi}\left[\sum_{j=1}^{3}\log\left(\frac{\|z - z_j\|^2}{(1 + \|z\|^2)(1 + \|z_j\|^2)}\right) + \frac{8\pi\omega_{\text{glob}}}{1 + \|z\|^2}\right]. \tag{14}$$

Hamilton's equations can be written compactly as

$$\dot{z}^* = -\mathrm{i}\frac{(1 + \|z\|^2)^2}{2}\frac{\partial H_p}{\partial z}, \tag{15}$$

where * denotes complex conjugation. These equations have a time reversal symmetry with reflection. If the initial isosceles

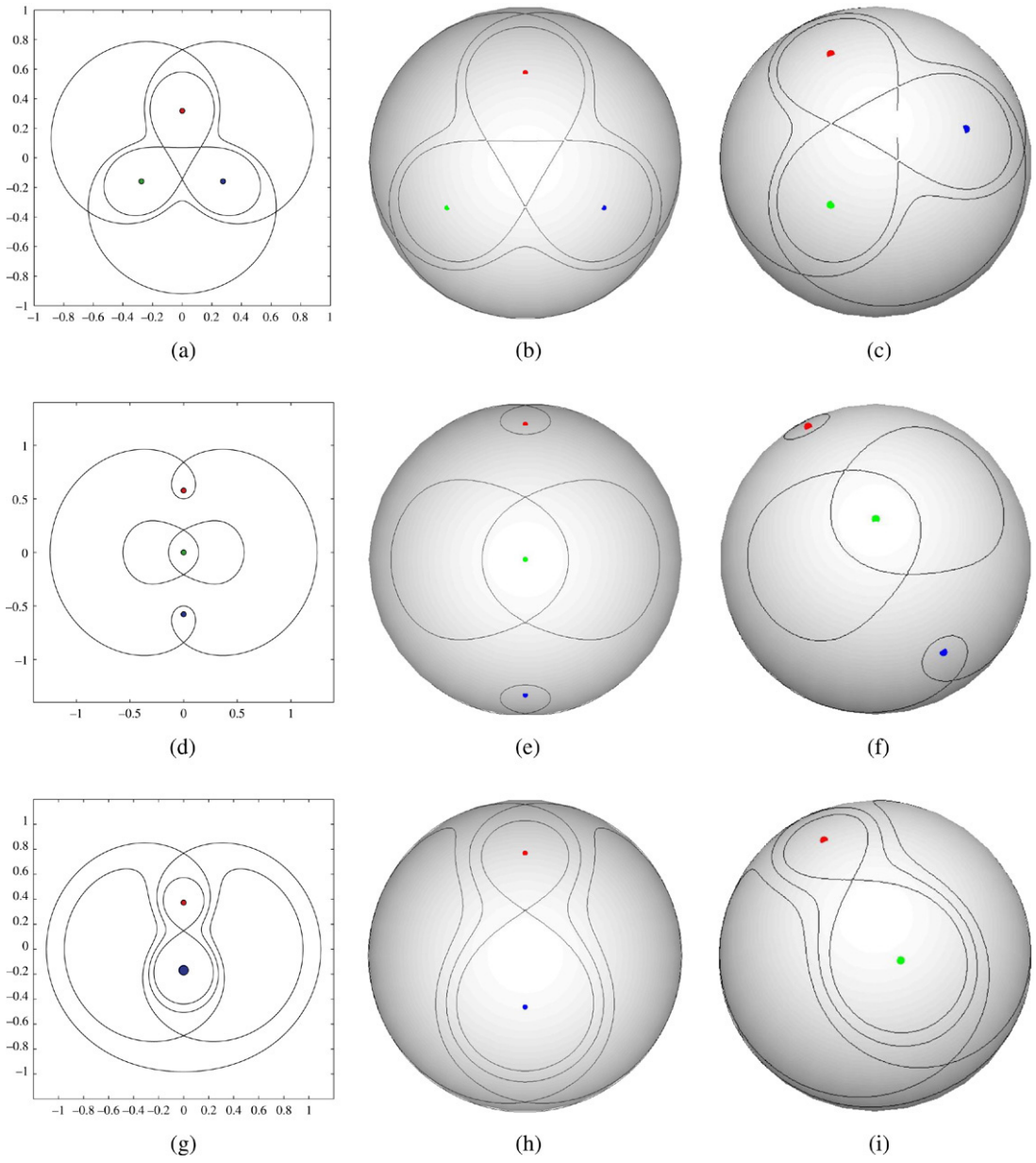

Fig. 7. Instantaneous streamlines in the co-rotating frame for $s = 1$ and $E = 0$ (first row), $E = E_c$ (second row) and $E = \infty$ (third row). The constant streamlines on the sphere are shown in a stereographic projection in the first column. The second and third columns show the streamlines on the sphere in a view from the north pole and from an angle, respectively.

triangle of vortices is symmetric about the real axis of $\mathcal{C}$, then for every solution $z(t)$, $-z^*(-t)$ is also a solution. This is because Eq. (15) is unchanged under the symmetry

$$z \to -z^*, \qquad t \to -t,$$

since

$$-z_1^*(-t) = z_1(t), \qquad -z_2^*(-t) = z_3(t),$$
$$-z_3^*(-t) = z_2(t).$$

The advection problem corresponds to a periodically forced Hamiltonian dynamical system. Because of the time dependence of H_p, the number of effective degrees of freedom is $1\frac{1}{2}$, allowing in general for chaotic motion. Note that H_p depends, in general, on the pair (s, E).

For the following study, we restrict ourselves to those cases of vortex motion with $s < \sqrt{3}$ for which the vortices never leave the northern hemisphere. For the special values of the vortex interaction energy $E = 0$ or $E = \infty$, the vortices are at a stable relative equilibrium and we have a stationary flow in the co-rotating system. The particle dynamics is nonchaotic, as the particles just follow streamlines (the $H_p = const$ curves). The case $E = E_c$ is also special, as we have a stationary flow, but an unstable one. The streamlines connected to saddle stagnation points for the steady flows of these three cases are shown in Fig. 7 for $s = 1$. As $s \to 0$, the curves in the first column look like the streamlines in the planar problem (see, e.g., [34]). Note that the cases $E = 0$, E_c and ∞ have six, four and three saddle points respectively.

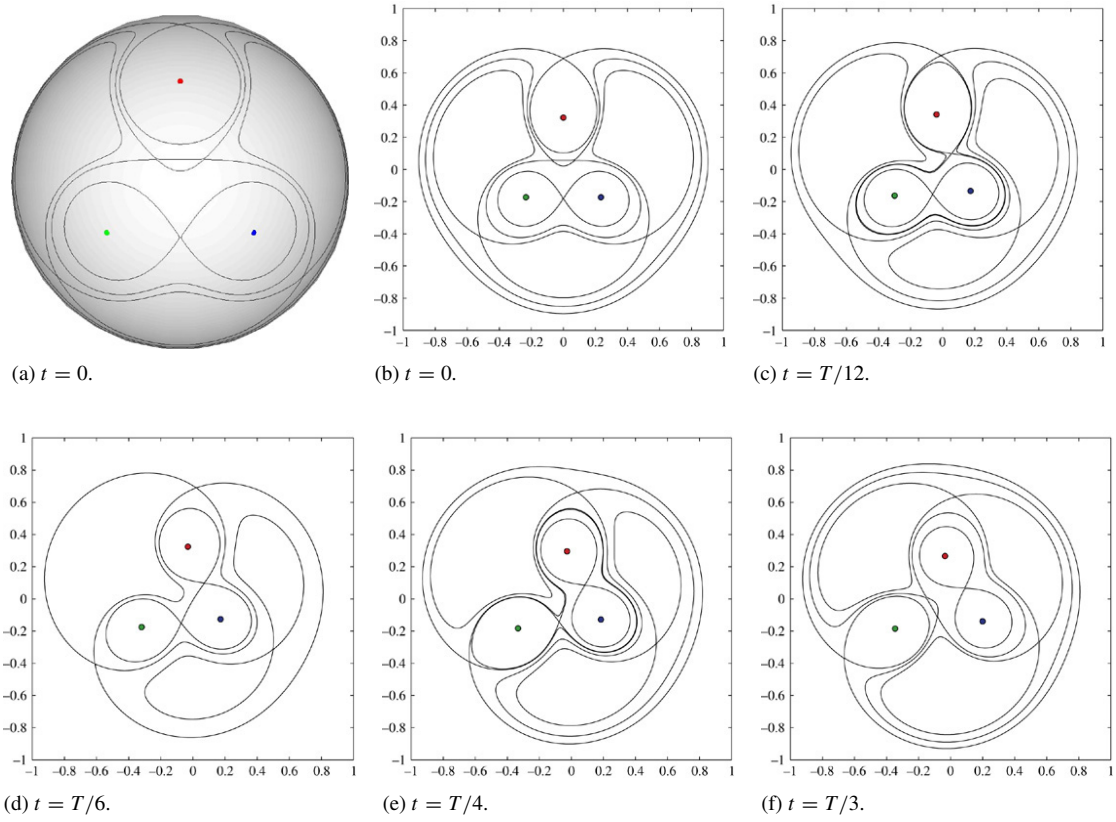

(a) $t = 0$. (b) $t = 0$. (c) $t = T/12$.

(d) $t = T/6$. (e) $t = T/4$. (f) $t = T/3$.

Fig. 8. Instantaneous streamlines in the co-rotating frame for $s = 1$ and $E = 0.01 \ll E_c$. The streamlines on the sphere for $t = 0$ are shown in (a) and the stereographic projection is shown at various times: (b) $t = 0$, (c) $t = T/12$, (d) $t = T/6$, (e) $t = T/4$, (f) $t = T/3$. Due to the permutation of the vortices, the relative motion is self-repeating for the rest of the period, with vortices permuted. We show only streamlines connected to saddle stagnation points. The vortices are shown as small circles. Note the change in streamline topology during the portion of the cycle shown. We see a change in vortex pairing: the bottom two vortices form a pair initially (a figure of eight streamline surrounds them both), but after the triplet halfway through the portion shown (at $t = T/6$), the upper two vortices form a pair.

3.3. Dynamically evolving streamline topologies

In general, the streamlines change periodically in time. In Fig. 8 we show the time dependence of instantaneous streamlines for a representative case of $0 < E \ll E_c$. We show only streamlines connected to saddle stagnation points: on the sphere in (a), and at various times in the stereographic projection in (b)–(f). Due to the permutation of the vortices, the relative motion is self-repeating for the rest of the relative motion period T, with vortices permuted. Thus we only show the streamlines up to $T/3$.

Notice that the streamline topology evolves dynamically. In particular, we can identify bifurcations from one pattern to another as the vortices evolve. At any given moment, the pattern of streamlines is made up of the building block patterns (or primitives) achievable on the sphere given in [24].

We see a change in vortex pairing: the bottom two vortices form a pair initially (a figure of eight streamline surrounds them both), but after the triplet halfway through the portion shown (at $t = T/6$), the upper two vortices form a pair.

In Fig. 8, a center and saddle near the origin merge at some time between (b) and (c) to form a cusp and then disappear altogether. The number of saddle points drops from six to five. The number of centers n_c (including the vortices) and that of saddles n_s are constrained by the Poincaré index theorem to be such that $n_c - n_s = 2$. This is why the center and saddle must merge and disappear, just as they emerge together again between (e) and (f) in the figure.

The case illustrated in Fig. 8 is the only example shown of a saddle–center merge and formation. The other cases have a constant number of saddle points throughout the vortex evolution. However, the number of saddle points depends on (s, E). For the remaining $s = 1$ cases shown in Figs. 9 and 10, there are four saddle points.

For all the cases, we notice that the number of critical streamlines reaches a minimum as they merge halfway through the portion of the cycle shown: at $T/6$ for $E < E_c$ and at $T/4$ for $E > E_c$. In Fig. 9, we do not have a center and saddle merging as was the case for $E = 0.01$. But we still see a change in vortex pairing. In Fig. 10, where the energy is above critical, there is no change in vortex pairing.

For $s = 1.5$, the $E = 0.2$ case has four saddle points, seen in Fig. 11. This case has the interesting feature that two streamlines seem to pass through each other near $t = 0.053T$, illustrated in (c). The limacon streamline attached to the bottom saddle point in (b) becomes a figure of eight (lemniscate) in (d). The streamline attached to the saddle point between the vortex pair and the upper vortex undergoes the reverse bifurcation. This bifurcation in streamline topology is not possible in the

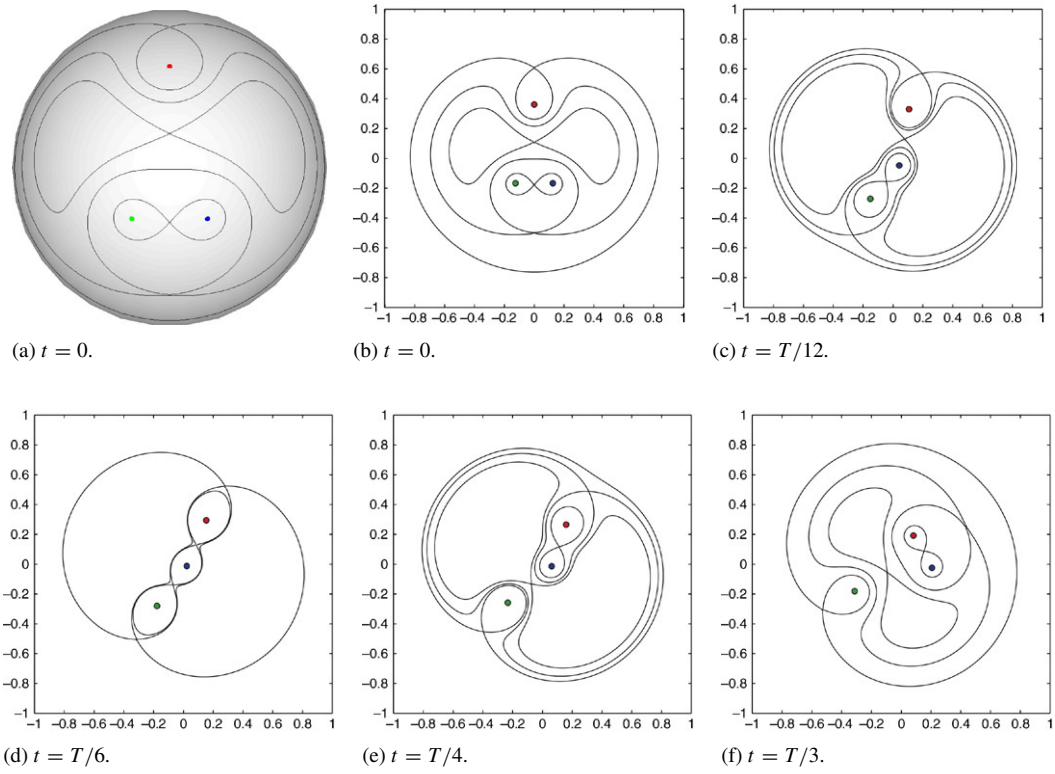

(a) $t = 0$. (b) $t = 0$. (c) $t = T/12$.

(d) $t = T/6$. (e) $t = T/4$. (f) $t = T/3$.

Fig. 9. Instantaneous streamlines in the co-rotating frame for $s = 1$ and $E = 0.29 < E_c$. The streamlines on the sphere for $t = 0$ are shown in (a) and the stereographic projection is shown at various times: (b) $t = 0$, (c) $t = T/12$, (d) $t = T/6$, (e) $t = T/4$, (f) $t = T/3$. As before, the relative motion is self-repeating for the rest of the period and we show only streamlines connected to saddle stagnation points. Vortex pair exchange occurs.

planar problem, being unique to the sphere, where the limacon is a homotopic equivalent to the lemniscate, i.e., they can be continuously deformed one into the other [24]. A similar bifurcation will occur between (e) and (f) at $t = T/3 - 0.053T$.

As we keep s fixed at 1.5 and increase the energy to 0.3, there are only three saddles. The case $E = 0.3$ is the only one where a stable island around a center near the south pole disappears, as will be shown below. As Fig. 12 shows, there are no bifurcations for this case, even though, as will be shown, this is the only case shown which allows transport between the north and south polar caps.

4. Mixing, transport, and ergodicity

4.1. Chaotic particle motion

For $s < \sqrt{3}$, besides the special cases ($E = 0, E_c, \infty$), we have a robust connected chaotic region on the sphere. In the hydrodynamical context, a strong mixing of the fluid takes place here, and therefore we will call such an extended chaotic region a mixing region. To visualize the particle dynamics we use a stroboscopic Poincaré map on which we represent the position of the particle on the co-rotating sphere taking snapshots with a time difference T, where $T = 2\pi/\omega_{\text{rel}}$ is the period of the forcing, i.e., the period of the relative motion of the vortices.

In Fig. 13 we show the stroboscopic maps for different representative energy values for $s = 1$. As can be seen, the area of the sphere occupied by the mixing region depends on E. The third column of Table 1 gives the fraction of the sphere occupied by the mixing region for each case shown in Figs. 13 and 14. This area is estimated using an equal-area box partition of the sphere and counting only those boxes which contain tracer particles. Tracers initially in the mixing region were followed for 2×10^5 iterates. Further details are in Section 5. When $E \ll E_c$ or $E \gg E_c$, the mixing region is restricted to the vicinity of the separatrices in the integrable cases. As we depart from these cases in energy, the mixing region extends significantly. The most extended chaotic mixing region for $s = 1$ seems to appear between $E = 0.29$ and 0.34, which are on either side of the critical energy. Note that for the critical energy, the stroboscopic map is undefined as T is infinite.

The relationship between the instantaneous streamlines and the mixing region can be seen for $E = 0.01$ in Fig. 13(a)–(d). For this energy, not too far from the equilateral triangle relative equilibrium, the mixing region covers over a third of the sphere. The region is roughly bounded by the saddle point streamlines for the six saddle points which exist for this case. There are stable regions around the vortices and the five other centers, including the largest at the south pole and a small zone near the north pole. However, some features are not captured by the streamlines, such as the two stable regions on the sides, one of which is shown in Fig. 13(c). This stable region is bounded below by a thin mixing strip which is part of the mixing region. How these other features arise is a question of future interest.

For $E = 0.60$ (Fig. 13(m)–(p)), we superimpose the streamlines corresponding to the two-vortex case, $E = \infty$.

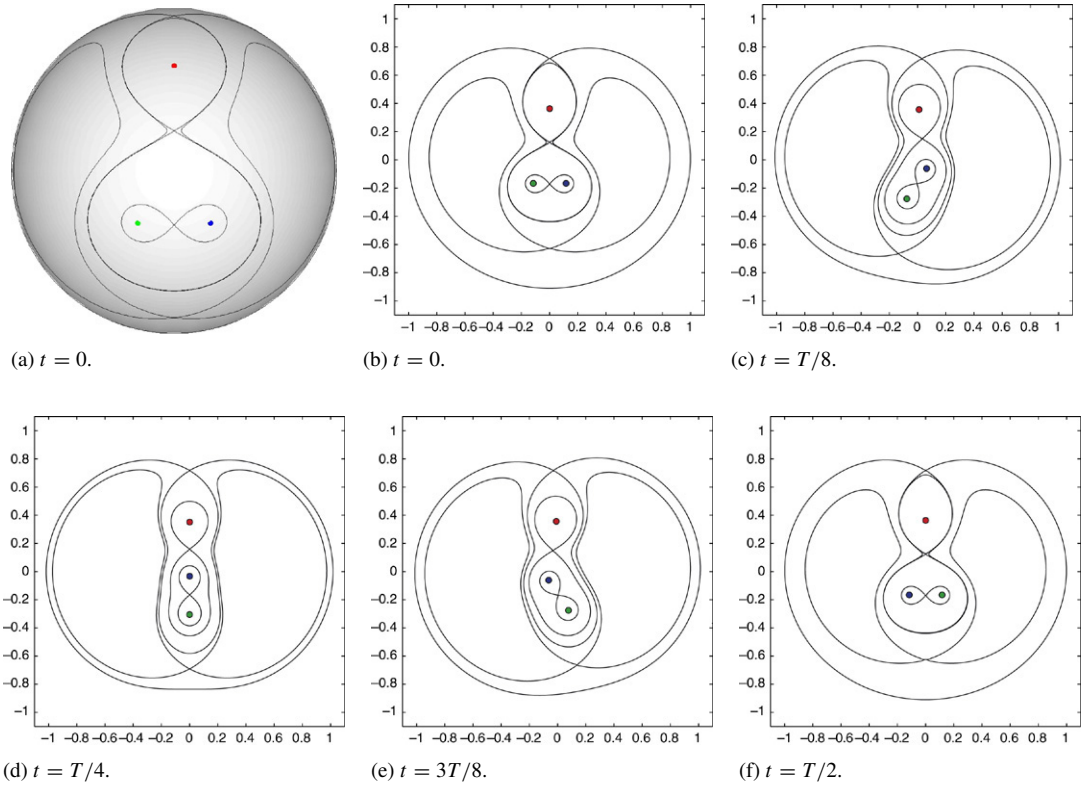

(a) $t = 0$. (b) $t = 0$. (c) $t = T/8$.

(d) $t = T/4$. (e) $t = 3T/8$. (f) $t = T/2$.

Fig. 10. Instantaneous streamlines in the co-rotating frame for $s = 1$ and $E = 0.34 > E_c$. The streamlines on the sphere for $t = 0$ are shown in (a) and the stereographic projection is shown at various times: (b) $t = 0$, (c) $t = T/8$, (d) $t = T/4$, (e) $t = 3T/8$, (f) $t = T/2$. As before, the relative motion is self-repeating for the rest of the period and we show only streamlines connected to saddle stagnation points. Notice that for this case of energy (above critical), there is no change in vortex pairing.

Table 1
Characteristics of the mixing region are shown for the eight cases illustrated in Figs. 13 and 14

s	E	Mixing region extent (%)	Spatial fraction in NH (%)	Time fraction in NH (%)
1	0.01	36.4 ± 1.2	86.0 ± 2.2	87.3
1	0.29	43.2 ± 1.0	100	100
1	0.34	39.4 ± 1.4	98.7 ± 1.3	99.9
1	0.60	17.9 ± 1.5	95.0 ± 5.0	93.3
1.5	0.1	79.0 ± 1.0	46.0 ± 0.7	39.0
1.5	0.2	82.1 ± 1.3	45.9 ± 0.6	46.4
1.5	0.3	74.9 ± 1.1	46.2 ± 0.7	44.3
1.5	0.6	17.7 ± 0.8	98.2 ± 1.8	97.2

The length parameter (s) and energy (E) label the cases. The third column shows the area of the mixing region as a percentage of the total sphere area, including an accuracy estimate. See Section 5 for the area estimation procedure. The fourth column shows the percentage of the mixing region which is in the northern hemisphere (NH) along with an accuracy estimate. The fifth column shows the fraction of time that a typical mixing region trajectory spends in the northern hemisphere. For this calculation, a trajectory of 2×10^5 iterates initialized in the mixing region was used. Note that spatial and time fractions are nearly equal, suggesting that the mixing region is nearly ergodic. The trajectory for the notable exception, $(s, E) = (1.5, 0, 1)$, got caught around a sticky island [32,26] forming the southern boundary in the southern hemisphere. For $(s, E) = (1, 0.29)$, the entire trajectory was in the NH.

This energy is large enough that the streamlines are relevant. Though the streamlines are not plotted for the remaining cases, the situation is similar: stable regions around the centers are seen.

At the energies shown in Fig. 13, the mixing region does not extend close to the point vortices or below a certain latitude near the equator. Each point vortex is surrounded by an island of regular motion, where advected particles are trapped. This behavior was noted in the planar case by, e.g., [3]. Note that for $E > E_c$, the two near vortices are surrounded by a common regular island. There are also regular islands which do not surround a vortex.

To illustrate the dependence of the mixing region size on s, we show the mixing region for representative energies for $s = 1.5$ in Fig. 14. For a given energy, the larger s system has smaller values for ω_{rel} and ω_{glob}. For this value, the mixing region does not seem to end near the equator but extends further south. There is a nonchaotic island around the south pole for energies $E = 0.1$ and 0.2 which gets smaller as the energy increases from $E = 0.1$ to 0.2. The $E = 0.2$ case also has

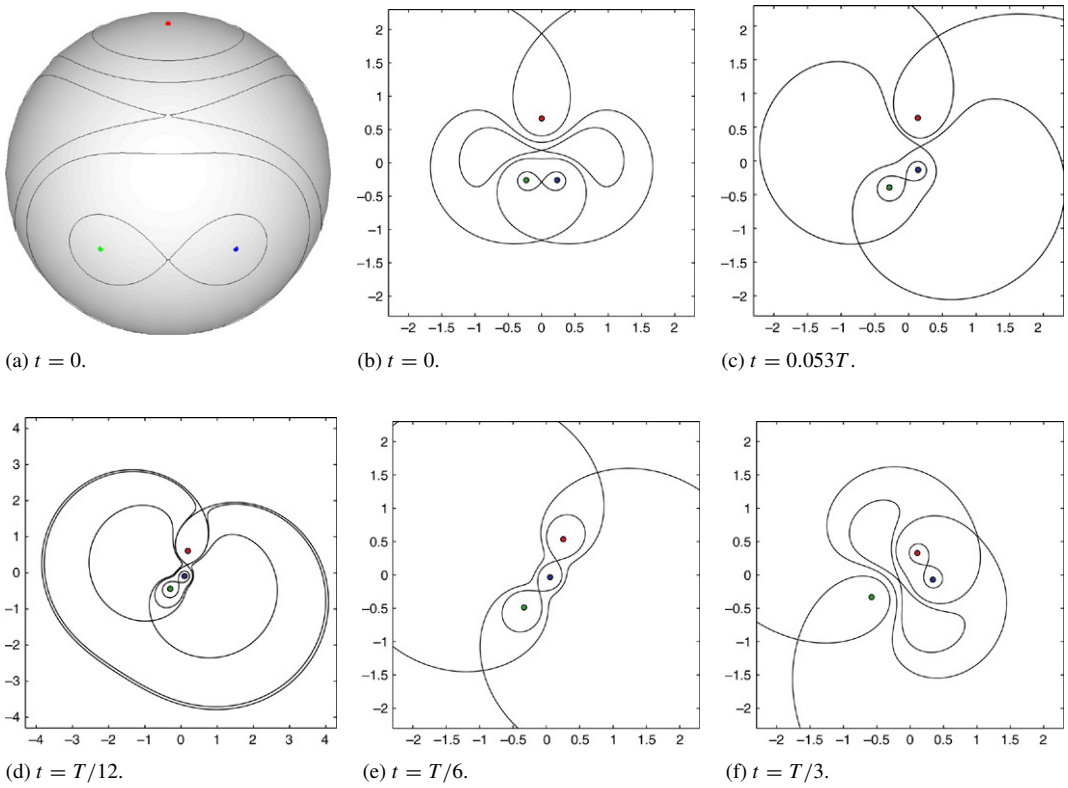

(a) $t = 0$. (b) $t = 0$. (c) $t = 0.053T$.

(d) $t = T/12$. (e) $t = T/6$. (f) $t = T/3$.

Fig. 11. Instantaneous streamlines in the co-rotating frame for $s = 1.5$ and $E = 0.2 < E_c$. The streamlines on the sphere for $t = 0$ are shown in (a) and the stereographic projection is shown at various times: (b) $t = 0$, (c) $t = 0.053T$, (d) $t = T/12$, (e) $t = T/6$, (f) $t = T/3$. As before, the relative motion is self-repeating for the rest of the period and we show only streamlines connected to saddle stagnation points. A unique case of streamlines passing through each other is shown in (c). The view is zoomed out in (d) to show the full streamlines, highlighting the interchange between limacon and lemniscate streamline curves, achievable only on the sphere as compared to the plane.

the largest mixing region of the cases surveyed, encompassing 82.1% of the sphere.

From Figs. 11 and 12 we see that the number of saddle stagnation points drops from four to three as we increase energy from 0.2 to 0.3. Three is the smallest number of all the example cases surveyed and interestingly, this is the only case where the mixing region encompasses the south pole. Transport between the north and south polar caps is possible, even though there is a small regular island near the north pole. For $E = 0.6$, that regular island grows in extent and encompasses the north pole. The mixing region decreases considerably, down to less than a quarter of the sphere. As we consider larger energies, the mixing region area shrinks to zero and the advection pattern approaches the regular advection in the field of two point vortices on the sphere with strengths Γ and 2Γ.

To illustrate the speed of mixing for the interesting case of $(s, E) = (1.5, 0.3)$ we consider a few iterates of a cap around the south pole. In Fig. 15(a), the boundary of an initial spherical cap at a latitude of 20° from the south pole (co-latitude $\theta = 160°$) is shown as a dashed line. The boundary is represented as a material line with particles placed along it. As the boundary is iterated, its resolution is preserved by adjusting the number and distribution of particles (e.g., by placing additional particles in regions of high curvature, [12, 17,45,27,11]). The second iterate of this boundary under the stroboscopic map is shown as a solid line in (a). Due to the area preservation of the stroboscopic map, the spherical areas of the cap and its iterates are equal. The accuracies of the area values are estimated as the difference in the area at each iterate n compared to the initial area, $a_0 = 2\pi(1 - \cos(20°))$, and are shown in the last column of Table 2. We can compare the area of the spherical cap with the overlap area of the cap and its iterates to determine the transport of an ensemble of particles out of the cap [29]. We can determine spherical areas bounded by curves using Green's Theorem for the sphere. We find that 67.04% of the particles initially in the cap (at $t = 0$) have escaped by the second iterate of the map, i.e., by $t = 2T$. All have escaped by the fourth iterate, shown in (b). In (c), a northern hemisphere view shows how the fourth iterate contains a long thin filament that weaves around the sphere. A similar phenomenon of thin spiral filaments has been seen in the transport of material out of polar vortex regions on Earth [20].

Due to the nearly ergodic nature of the mixing region, particles which escape the cap are likely to return intermittently. Within a few more iterates, some portion of the area will intersect the initial cap. This intersection region will subsequently get folded and stretched, a basic mechanism for the generation of chaos.

We can get a better handle on the features of the flow which control transport by considering Fig. 16 showing the area bounded by the fourth iterate of the cap in a stereographic projection along with the instantaneous streamlines. The arrows on the streamlines indicate the flow direction. As these streamlines are attached to saddle stagnation points, they are

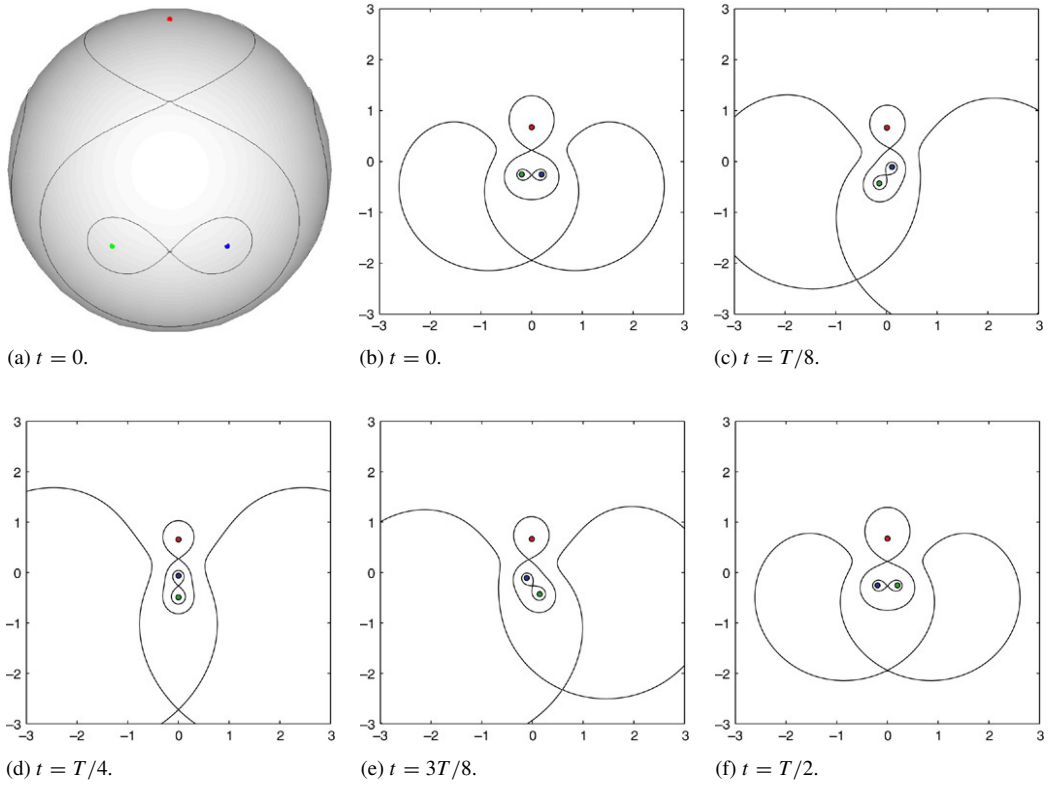

(a) $t = 0$. (b) $t = 0$. (c) $t = T/8$.

(d) $t = T/4$. (e) $t = 3T/8$. (f) $t = T/2$.

Fig. 12. Instantaneous streamlines in the co-rotating frame for $s = 1.5$ and $E = 0.3 > E_c$. The streamlines on the sphere for $t = 0$ are shown in (a) and the stereographic projection is shown at various times: (b) $t = 0$, (c) $t = T/8$, (d) $t = T/4$, (e) $t = 3T/8$, (f) $t = T/2$. As before, the relative motion is self-repeating for the rest of the period and we show only streamlines connected to saddle stagnation points. There is no change in vortex pairing.

Table 2
Change in arc length of a material boundary is shown for the spherical cap and its images shown in Fig. 15

n	Boundary length	Stretching rate	Area error
0	1	n/a	n/a
1	1.1482	1.1482	1×10^{-10}
2	2.0095	1.7502	3×10^{-8}
3	4.8643	2.4206	2×10^{-6}
4	31.7483	6.5268	9×10^{-4}

The arc lengths have been normalized by dividing by the initial area. The stretching rates give the ratio of the boundary length at iterate n to that at $n-1$ for $n \geq 1$. The error in the area at each n (compared to the initial area) is given in the final column to indicate the accuracy of the computation.

approximations of the stable and unstable manifolds of those points. Stretching along the unstable directions is seen. The long and folded area weaves around the manifolds of more than one saddle point, leading to its complicated shape.

The change in the arc length of the boundary of the cap is shown in Table 2 for iterates $n = 0, \ldots, 4$. The arc lengths have been normalized by dividing by the initial boundary length, $l_0 = 2\pi \sin(20°)$. The stretching of the boundary is equivalent to a weight average of finite-time Lyapunov exponents over the set of particles distributed along it [15,9]. The stretching rate is increasing monotonically as the blob of fluid gets entrained in the region between the vortices.

For a given size of south polar cap, we ask what is the minimum number of iterates necessary to reach a north polar cap. Continuing the current example for a 20° south polar cap, let us consider the time it takes to reach a 2° north polar cap. We find the third backward iterate intersects the fourth forward iterate of the south polar cap, as shown in Fig. 17. Thus, for the sizes of caps used here, it takes only seven iterates for some particles in the south polar cap to reach the north polar cap.

5. Numerical procedures

We describe briefly in this section some of the numerical procedures used. Many of the procedures are novel implementations of algorithms currently under development in other contexts that required significant modification based on the spherical geometry of the problem.

5.1. Measuring the extent of the mixing region

The extent of the mixing region can be measured using a box counting approximation [11]. This approach is also coarse-grained, but does not require the explicit calculation of regular island boundaries. It requires only that we have a sufficient number of marks of tracer particles spread throughout the Poincaré section to adequately approximate the area. It is a quantitative extension of the qualitative pictures given by tracer clouds in stroboscopic maps, as in Figs. 13 and 14.

5.2. Equal-area box partition

The flow field, in this case the sphere S^2, is partitioned into small boxes, or subsets. The problem of choosing the best

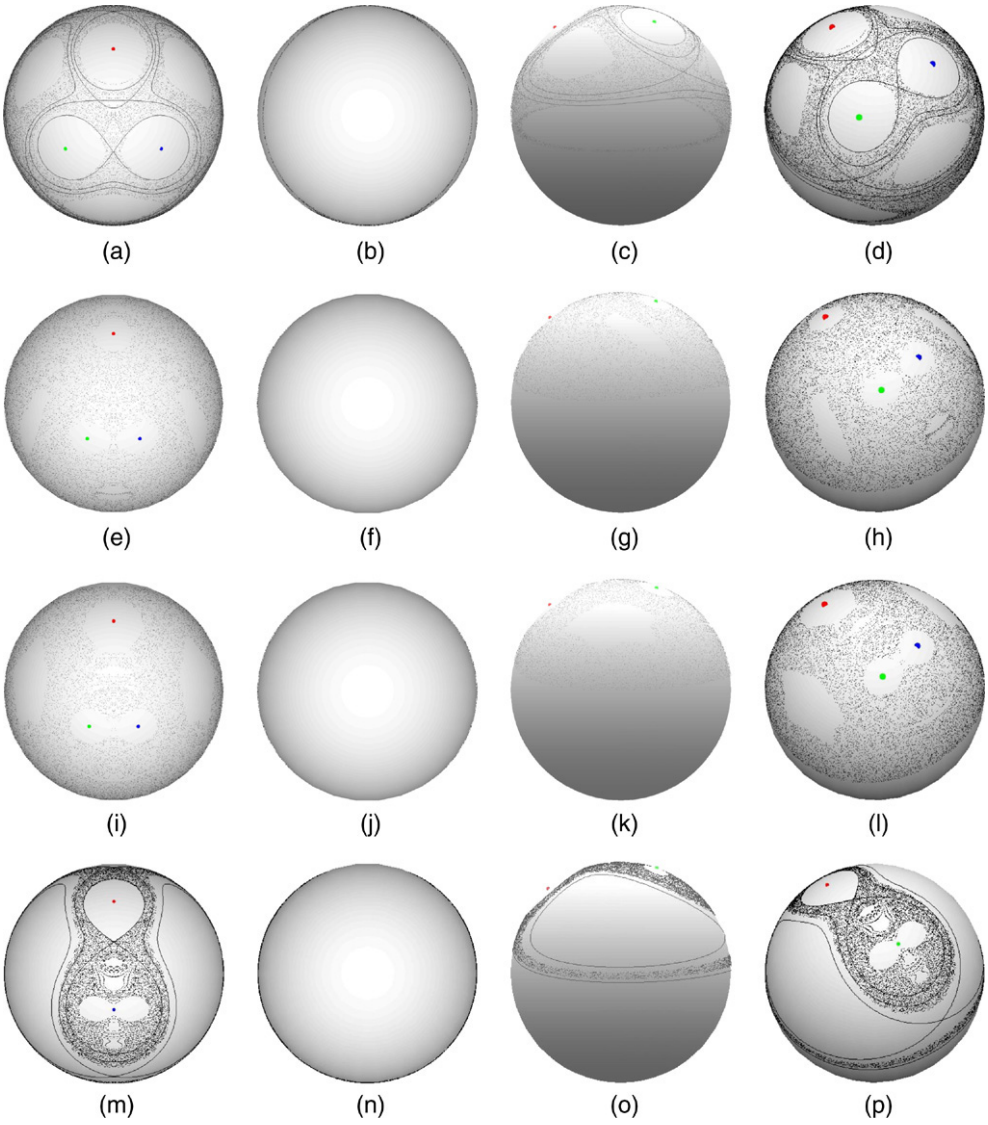

Fig. 13. Stroboscopic maps obtained by trajectories in the mixing region of the flow for $s = 1$ and (a)–(d) $E = 0.01$, (e)–(h) $E = 0.29$, (i)–(l) $E = 0.34$, (m)–(p) $E = 0.60$. Dots represent intersections with the Poincaré plane for a single chaotic tracer trajectory starting at the north pole. About 10^4 tracer points are shown for each energy. From left to right, the views are from the north pole, south pole, the side, and from an angle, respectively. For the $E = 0.01$ case, we show the streamlines for this energy superimposed. For the $E = 0.60$ case, we superimpose the $E = \infty$ streamlines.

box covering of the sphere is an unsolved problem related to distributing a large number of points uniformly on the sphere [31,33,21] — Smale's 7th problem for the twenty-first century [44]. As the flow field we are studying is area preserving, we choose a partitioning of the sphere into n_b equal-area parts with small diameters [39]. For simplicity, we use spherical coordinates, and denote the $n_b = n_\theta \times n_\phi$ subsets as $D_{11}, D_{12}, \ldots, D_{n_\theta n_\phi}$. Lebesgue (area) measure on S^2 is denoted by σ, so that $\sigma(S^2) = 4\pi$. Our partition is such that

$$\bigcup_{i,j} D_{ij} = S^2,\ D_{ij} \cap D_{kl} \text{ has empty interior if } i \neq k \text{ and } j \neq l,$$
$$\sigma(D_{ij}) = 4\pi/n_b.$$

Each D_{ij} is a square on the sphere bounded by two constant co-latitude lines and two constant longitude lines,

$$D_{ij} = [\theta_{i-1}, \theta_i] \times [\phi_{j-1}, \phi_j].$$

In spherical coordinates, the area element is

$$\mathrm{d}\sigma = \sin(\theta)\mathrm{d}\theta\mathrm{d}\phi.$$

Integrating over D_{ij}, we have

$$\begin{aligned}\sigma(D_{ij}) &= \int_{D_{ij}} \mathrm{d}\sigma,\\ &= \int_{\phi_{j-1}}^{\phi_j}\int_{\theta_{i-1}}^{\theta_i} \sin(\theta)\mathrm{d}\theta\mathrm{d}\phi,\\ &= \delta\phi \int_{\theta_{i-1}}^{\theta_i} \sin(\theta)\mathrm{d}\theta,\end{aligned}$$

where $\delta\phi = \int_{\phi_{j-1}}^{\phi_j} \mathrm{d}\phi$ is the constant angular spacing between longitude lines. These lines are given by $\phi_0 = 0$, $\phi_j = \phi_{j-1} + \delta\phi$, $j = 1, \ldots, n_\phi$, where $\delta\phi = 2\pi/n_\phi$. In order to

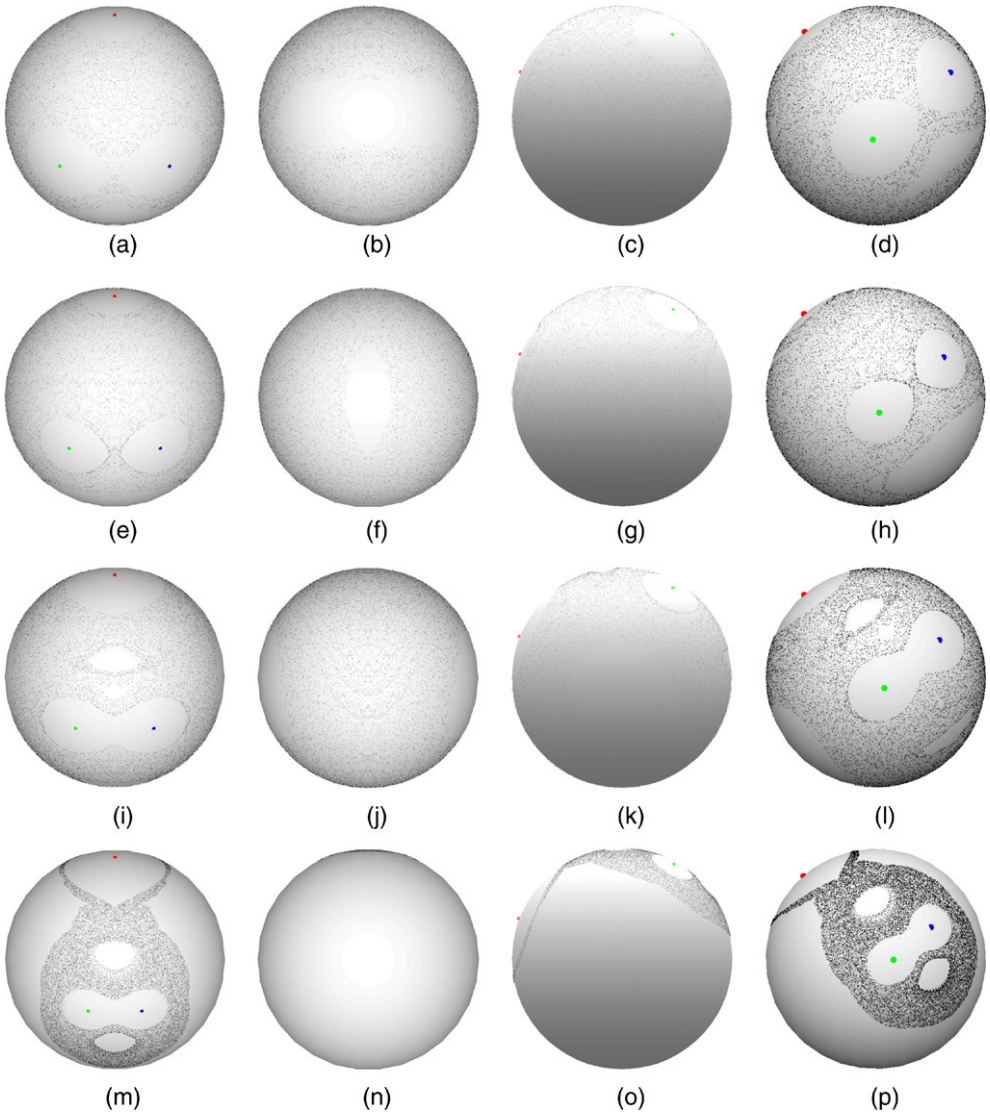

Fig. 14. Stroboscopic maps obtained by trajectories in the mixing region of the flow for $s = 1.5$ and (a)–(d) $E = 0.1$, (e)–(h) $E = 0.2$, (i)–(l) $E = 0.3$, (m)–(p) $E = 0.6$. The particles for $E = 0.1$ to 0.3 began at the north pole, while for $E = 0.6$ the particle began at a co-latitude of 20°. The views are the same as in Fig. 13. About 10^4 tracer points are shown for each energy. Note the larger extent of the mixing region compared with those for $s = 1$ in Fig. 13. For $E = 0.3$, the transport between the north pole and south pole is possible. For $E = 0.6$ there is an elliptic island encompassing the north pole.

have $\sigma(D_{ij}) = 4\pi/n_b$, we need

$$\int_{\theta_{i-1}}^{\theta_i} \sin(\theta)\mathrm{d}\theta = \frac{4\pi}{n_b \delta\phi}, \\ = \frac{2}{n_\theta}.$$

The co-latitude lines are not equally spaced in θ for $n_\theta \geq 3$. They are given by $\theta_0 = 0$ and $\cos(\theta_i) = \cos(\theta_{i-1}) - 2/n_\theta$, $i = 1, \ldots, n_\theta$.

For a given n_b, we want to pick the ratio of n_ϕ/n_θ appropriately. We can determine this by setting the edge lengths to be nearly equal near the equator. For boxes near the equator, $\sin(\theta) \approx 1$, so $\int_{\theta_{i-1}}^{\theta_i} \sin(\theta)\mathrm{d}\theta$ is approximately the length of the longitude sides of the box, $\delta\theta_{\mathrm{eq}}$. Requiring $\delta\theta_{\mathrm{eq}} \approx \delta\phi$ gives us $n_\phi = \lfloor \pi n_\theta \rfloor$, where $\lfloor x \rfloor$ denotes the largest integer not greater than x.

Let $P = \{p_1, p_2, \ldots, p_N\}$ denote the collection of N tracer points on the sphere. P could be a cloud of tracer particles initialized in the mixing region and followed for long times to approximate the mixing region. Then let $\overline{\mathcal{M}} = \{D_{ij}\}$ denote the box collection of all D_{ij} such that $P \bigcap D_{ij} \neq \emptyset$. In other words, we keep boxes that contain points in the mixing region and discard the others. An upper bound on the area of the mixing region is then given by $\sigma(\overline{\mathcal{M}})$.

5.3. Adequate resolution

To obtain adequate spatial resolution of the mixing region given a scattering of only N tracer points spread about the sphere, we need to pick n_b appropriately. This is a difficult problem. We do not want boxes so large that we grossly overestimate the mixing region extent. However, boxes which are too small will grossly underestimate the mixing region. If

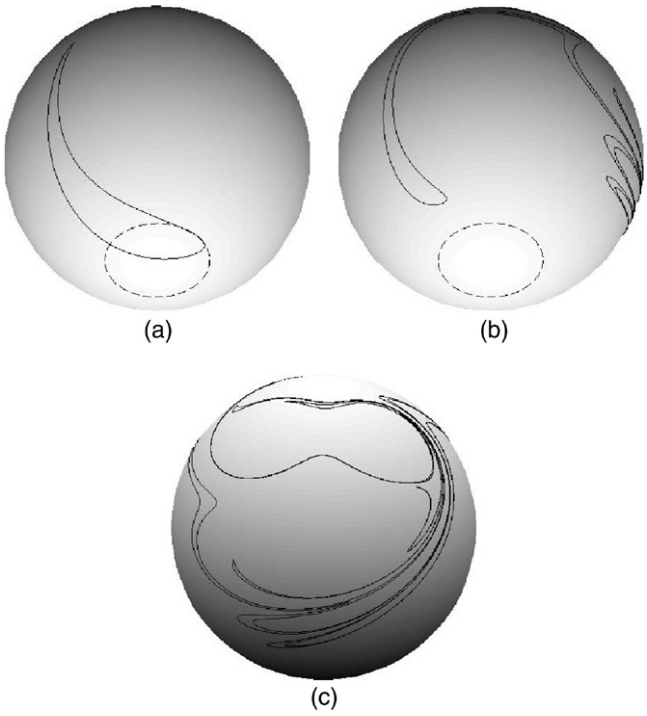

Fig. 15. The boundary of a spherical cap around the south pole (dashed in (a) and (b)) and some iterates under the stroboscopic map are shown. (a) The second iterate is shown as a solid curve in this southern hemisphere view. (b) The fourth iterate is shown. (c) Another view of the fourth iterate, showing the northern hemisphere.

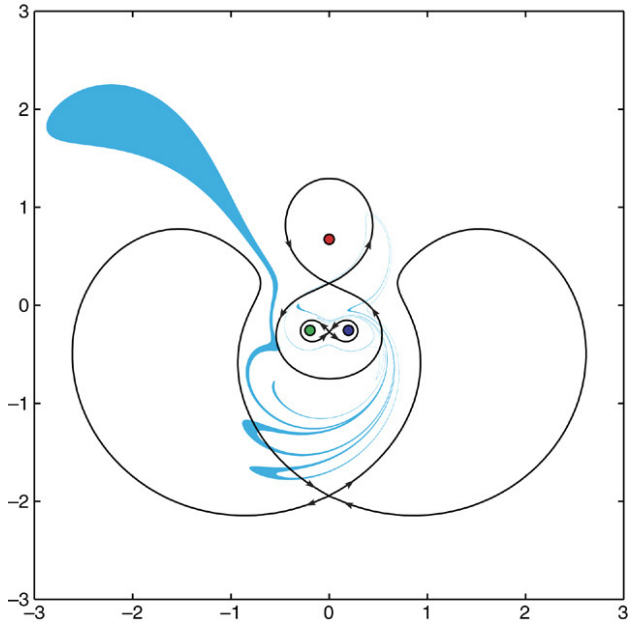

Fig. 16. The area bounded by the fourth iterate of a south polar spherical cap is shown in this stereographic projection along with the instantaneous streamlines with flow arrows.

the N tracer points were distributed uniformly over the sphere, they would each occupy an area of $4\pi/N$ which we take as our minimum scale $\alpha_{\min}$. As all the mixing regions measured did not cover the entire sphere (e.g., the islands surrounding the vortices in Figs. 13 and 14 are excluded), this is an upper bound

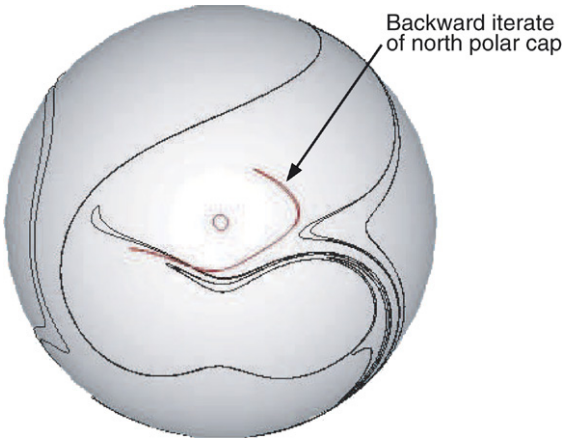

Fig. 17. The third backward iterate of a small north polar cap is shown along with the fourth iterate of the south polar cap shown previously in Fig. 15(c). The north polar cap is the small circle at the center and its third backward iterate is the curve right of center which intersects the south polar cap fourth iterate.

on the average area surrounding each tracer point. We want the boxes of our partition to be able to pick up features of this scale, i.e., $\sigma(D_{ij}) > \alpha_{\min}$. Thus, we want $n_b = \lfloor N/k \rfloor$, where $k > 1$. On the basis of numerical experimentation, we find using $k = 5$ works well for $N \approx 10^5$, yielding a close bracketing of the supposed true area value (see the next paragraph). In Fig. 18, we show the box covering $\overline{\mathcal{M}}$ of $N = 2 \times 10^5$ mixing region tracers from Fig. 14(i)–(l) using $k = 50$ (a) and $k = 5$ (b). A visual inspection reveals that the mixing region is fairly well covered, even in (a). At least one regular island is discernible in the lower right of (a) which is not picked up at the $k = 50$ resolution, revealing the approximate nature of the covering.

5.4. Accuracy

The accuracy of $\overline{\mathcal{M}}$ as a covering of the mixing region can be gauged by measuring the difference between the area of $\overline{\mathcal{M}}$ and $\underline{\mathcal{M}}$, where $\underline{\mathcal{M}} = \overline{\mathcal{M}} \setminus \partial\mathcal{M}$ and $\partial\mathcal{M}$ contains boxes on the boundary of $\overline{\mathcal{M}}$. Considering Fig. 18, the boxes contained in $\partial\mathcal{M}$ are those surrounding the white regular regions. The region $\underline{\mathcal{M}}$ is then entirely contained within the mixing region. The areas of two regions, $\sigma(\overline{\mathcal{M}})$ and $\sigma(\underline{\mathcal{M}})$, should bracket the true value of the mixing region, $\sigma(\mathcal{M})$. For the area measurements given in Table 1, we used an average,

$$\sigma(\mathcal{M}) = \frac{1}{2}\left(\sigma(\overline{\mathcal{M}}) + \sigma(\underline{\mathcal{M}})\right),$$

where the accuracy is estimated as $\frac{1}{2}\sigma(\partial\mathcal{M})$. The choice mentioned above of $k = 5$ yields accuracies of about 1% when using $N \approx 10^5$. The actual accuracy value depends on how large the boundaries are, or in other words, how many holes are in the mixing region. The number of holes changes in a complicated fashion with s and E.

A similar procedure, restricted to the northern hemisphere, yields area estimates for the portion of the mixing region in that hemisphere in the fourth column of Table 1.

Extensions of this method to systematically increase the accuracy are needed. One approach applied to other problems of physical interest is to use adaptive box sizes, using,

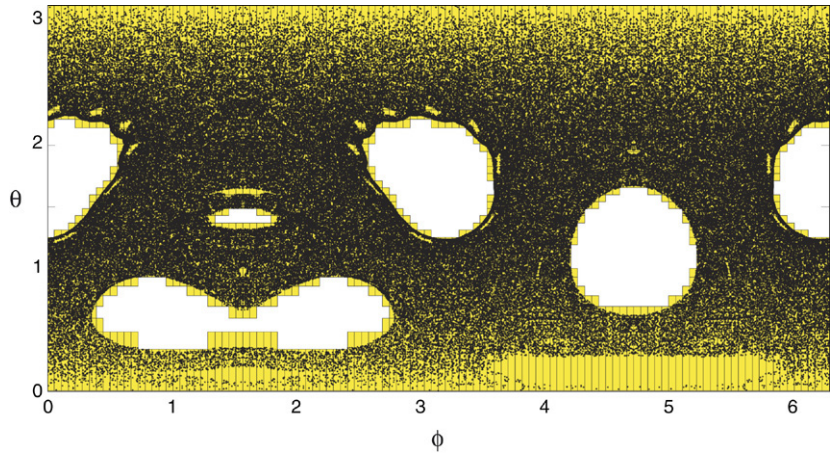

(a) $k = 50$, 4000 boxes.

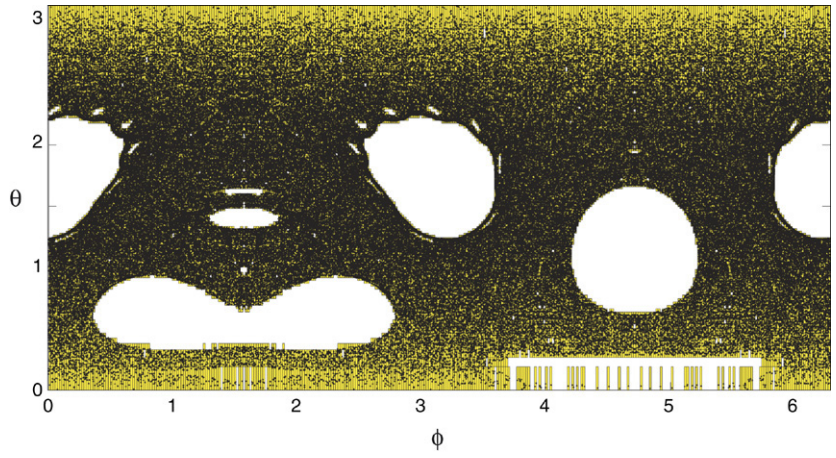

(b) $k = 5$, 40000 boxes.

Fig. 18. Box covering $\overline{\mathcal{M}}$ of $N = 2 \times 10^5$ mixing region tracers from Fig. 14(i)–(l), where $s = 1.5$, $E = 0.3$. The initial box covering consists of about (a) 4000 boxes and (b) 40 000 boxes. The boxes in the upper and lower figures have equal area on the sphere, but their projections in spherical coordinates are smallest near the equator and largest near the poles.

for example, efficient box subdivision algorithms along the boundary $\partial\mathcal{M}$ [11].

6. Discussion and conclusions

The analysis performed in this paper of advection in the flow field of three identical point vortices on the sphere has illuminated a number of features which should be relevant in the case of more general vortex-dominated flows on the sphere. The case of three-vortex flow, as in the planar problem, is a special case as it is the simplest such system generating Lagrangian chaos. The motion of the vortices is in general quasi-periodic, characterized by a frequency of relative motion of the vortices and a global rotation of the vortices about the center of vorticity vector. We parametrize the three-vortex motion by an interaction energy and a characteristic length scale, related to the average distance between the vortices compared to the diameter of the sphere.

The vortex interaction energy naturally divides the advection phase space for a tracer particle into two regimes of motion: (a) sequential pairing between the three vortices, i.e., partner exchange, and (b) two of the vortices form a pair which wrap around each other for all time.

Using a stroboscopic map (at the vortex relative motion frequency), we find the phase space of the advected particle contains a large connected chaotic component, the mixing region. The mixing region area is estimated using an equal-area box partition of the sphere and counting only those boxes which contain tracer particles. The mixing region covers the largest portion of the sphere for energies on either side of the critical energy, which corresponds to an unstable great circle equilibrium. Computational evidence suggests the mixing region is, for all practical purposes, ergodic. For some energy ranges, particles in the north polar cap (defined by the center of vorticity vector) can wander to the south polar cap, and vice versa, via small-scale filamentary structures.

The instantaneous streamline patterns of the three-vortex flow field undergo topological bifurcations both as a function of energy and during the course of their evolution for fixed energy values. Some bifurcations involve formation and disappearance of stagnation points while respecting the constraints imposed by the Poincaré index theorem [35]. Others involve homotopies

due to the spherical topology. The streamline patterns reveal some of the gross features of the phase space, particularly the location of islands around centers.

Advection in a multi-vortex flow on a sphere provides an important link between simple dynamical systems models and much more complicated models of particle advection in global geophysical flows, such as the polar vortex [16,43]. Taking the point of view of building dynamically consistent simple models, we can add additional vortices of various strengths, along with realistic rotation models, all of which avoids the trouble of interpreting results belonging only to a kinematic model [15]. The flow field in the presence of four or more vortices on the sphere will have general time dependence and other techniques for quantifying transport can be used [14, 19,27,28,41], but the qualitative picture from the three-vortex model can serve as a useful guide.

Acknowledgments

SDR would like to thank Frederic Gabern for discussions regarding optimal distributions of points on the sphere. This work was supported by the National Science Foundation grants NSF-DMS 0402842 (SDR), NSF-DMS 9800797 (PKN) and NSF-DMS 0203581 (PKN).

References

[1] The Antarctic stratospheric sudden warming and split ozone hole of 2002, J. Atmos. Sci. 62 (3) (2005) (special issue) Allen Press.
[2] H. Aref, P.K. Newton, M. Stremmler, T. Tokieda, D. Vainchtein, Vortex crystals, Adv. Appl. Math. 39 (2002) 1–79.
[3] A. Babiano, G. Boffetta, A. Provenzale, A. Vulpiani, Chaotic advection in point vortex models and two-dimensional turbulence, Phys. Fluids 6 (7) (1994) 2465–2474.
[4] S. Boatto, H.E. Cabral, Nonlinear stability of a latitudinal ring of point vortices on the nonrotating sphere, SIAM J. Appl. Math. 64 (1) (2003) 216–230.
[5] V.A. Bogomolov, Two-dimensional fluid dynamics on a sphere, Izv. Atmos. Ocean. Phys. 15 (1) (1979) 18–22.
[6] A.V. Borisov, A.E. Pavlov, Dynamics and statics of vortices on a plane and a sphere I, Regul. Chaotic Dyn. 3 (1) (1998) 28–38.
[7] A.V. Borisov, V.G. Lebedev, Dynamics and statics of vortices on a plane and a sphere II, Regul. Chaotic Dyn. 3 (2) (1998) 99–114.
[8] A.V. Borisov, V.G. Lebedev, Dynamics and statics of vortices on a plane and a sphere III, Regul. Chaotic Dyn. 3 (4) (1998) 74–86.
[9] K.P. Bowman, Barotropic simulation of large-scale mixing in the Antarctic polar vortex, J. Atmos. Sci. 50 (1993) 2901–2914.
[10] P. Boyland, M. Stremler, H. Aref, Topological fluid mechanics of point vortex motions, Physica D 175 (2003) 69–95.
[11] M. Dellnitz, O. Junge, W.-S. Koon, F. Lekien, M.W. Lo, J.E. Marsden, K. Padberg, R. Preis, S.D. Ross, B. Thiere, Transport in dynamical astronomy and multibody problems, Int. J. Bifurc. Chaos 15 (3) (2005) 699–727.
[12] D.G. Dritschel, Contour dynamics and contour surgery: numerical algorithms for extended, high-resolution modelling of vortex dynamics in two-dimensional, inviscid, incompressible flows, Comput. Phys. Rep. 10 (1989) 77–146.
[13] G. Gómez, W.S. Koon, M.W. Lo, J.E. Marsden, J. Masdemont, S.D. Ross, Connecting orbits and invariant manifolds in the spatial restricted three-body problem, Nonlinearity 17 (2004) 1571–1606.
[14] G. Haller, G. Yuan, Lagrangian coherent structures and mixing in two-dimensional turbulence, Physica D 147 (2000) 352–370.
[15] P. Haynes, Transport, stirring and mixing in the atmosphere, in: H. Chaté, E. Villermaux (Eds.), Proceedings of the NATO Advanced Study Institute on Mixing: Chaos and Turbulence, Cargese, Corse, France, 7–20 July, 1996, Kluwer, 1999, pp. 229–272.
[16] P. Haynes, Stratospheric dynamics, Annu. Rev. Fluid Mech. 37 (2005) 263–293.
[17] D. Hobson, An efficient method for computing invariant manifolds of planar maps, J. Comput. Phys. 104 (1993) 14–22.
[18] M.I. Jamaloodeen, P.K. Newton, The N-vortex problem on a rotating sphere II. Heterogeneous Platonic solid equilibria, Proc. R. Soc. Lond. Ser. A 2007 (in press).
[19] C.K.R.T. Jones, S. Winkler, Invariant manifolds and Lagrangian dynamics in the ocean and atmosphere, in: B. Fiedler (Ed.), Handbook of Dynamical Systems, vol. 2, Elsevier, 2002, pp. 55–92.
[20] M.N. Juckes, M.E. McIntyre, A high-resolution one-layer model of breaking planetary waves in the stratosphere, Nature 328 (1987) 590–596.
[21] J.L. Junkins, P. Singla, How nonlinear is it? A tutorial on nonlinearity of orbit and attitude dynamics, J. Astron. Sci. 52 (1–2) (2004) 7–60.
[22] R. Kidambi, P.K. Newton, Motion of three point vortices on a sphere, Physica D 116 (1998) 143–175.
[23] R. Kidambi, P.K. Newton, Collision of three vortices on a sphere, Nuovo Cimento C 22 (6) (1999) 779–791.
[24] R. Kidambi, P.K. Newton, Streamline topologies for integrable vortex motion on a sphere, Physica D 140 (2000) 95–125.
[25] W.S. Koon, M.W. Lo, J.E. Marsden, S.D. Ross, Heteroclinic connections between periodic orbits and resonance transitions in celestial mechanics, Chaos 10 (2000) 427–469.
[26] L. Kuznetsov, G.M. Zaslavsky, Passive particle transport in three-vortex flow, Phys. Rev. E 61 (4) (2000) 3777–3792.
[27] F. Lekien, Time-dependent dynamical systems and geophysical flows, Ph.D. Thesis, California Institute of Technology, 2003.
[28] F. Lekien, C. Coulliette, J.E. Marsden, Lagrangian structures in high-frequency radar data and optimal pollution timing, in: Proceedings of the 7th Experimental Chaos Conference, Ameri. Inst. Phys, 2003, pp. 162–168.
[29] F. Lekien, J.E. Marsden, S.D. Ross, Lobes and lobe areas, 2006 (in preparation).
[30] C.C. Lim, J. Montaldi, M. Roberts, Relative equilibria of point vortices on the sphere, Physica D 148 (2001) 97–135.
[31] G. Marsaglia, Choosing a point from the surface of a sphere, Ann. Math. Statist. 43 (2) (1972) 645–646.
[32] J.D. Meiss, Symplectic maps, variational principles, and transport, Rev. Modern Phys. 64 (3) (1992) 795–848.
[33] T.W. Melnyk, O. Knop, W.R. Smith, Extremal arrangements of points and unit charges on a sphere: equilibrium configurations revisited, Canad. J. Chem. 55 (10) (1977) 1745–1761.
[34] Z. Neufeld, T. Tél, The vortex dynamics analogue of the restricted three-body problem: Advection in the field of three identical point vortices, J. Phys. A: Math. Gen. 30 (1997) 2263–2280.
[35] P.K. Newton, The N-Vortex Problem: Analytical Techniques, in: Appl. Math. Sci. Series, vol. 145, Springer-Verlag, Berlin, Heidelberg, New York, 2001.
[36] P.K. Newton, H. Shokraneh, The N-vortex problem on a rotating sphere I. Multi-frequency configurations, Proc. R. Soc. Lond. Ser. A 462 (2006) 149–169.
[37] S. Pekarsky, J.E. Marsden, Point vortices on a sphere: Stability of relative equilibria, J. Math. Phys. 39 (1998) 5894–5907.
[38] L. Polvani, D.G. Dritschel, Wave and vortex dynamics on the surface of a sphere, J. Fluid Mech. 255 (1993) 35–64.
[39] E.B. Saff, A.B.J. Kuijlaars, Distributing many points on a sphere, Math. Intelligencer 19 (1) (1997) 5–11.
[40] T. Sakajo, The motion of three point vortices on a sphere, Japan J. Indust. Appl. Math. 16 (1999) 321–347.
[41] S.C. Shadden, F. Lekien, J.E. Marsden, Definition and properties of Lagrangian coherent structures: Mixing and transport in two-dimensional aperiodic flows, Physica D 212 (2005) 271–304.
[42] H. Shokraneh, Ph.D. Thesis, Department of Aerospace and Mechanical Engineering, University of Southern California, 2006.

[43] A. Simmons, M. Hortal, G. Kelly, A. McNally, A. Untch, S. Uppala, ECMWF analyses and forecasts of stratospheric winter polar vortex break-up: September 2002 in the southern hemisphere and related events, J. Atmos. Sci. 62 (3) (2005) 668–689.
[44] S. Smale, Mathematical problems for the next century, Math. Intelligencer 20 (2) (1998) 7–15.
[45] D.W. Waugh, R.A. Plumb, R.J. Atkinson, M.R. Schoeberl, L.R. Lait, P.A. Newman, M. Loewenstein, D.W. Toohey, L.M. Avallone, C.R. Webster, R.D. May, Transport out of the lower stratospheric arctic vortex by Rossby wave breaking, J. Geophys. Res. 99 (D1) (1994) 1071–1088.